The Annual Wind-driven Rossby Wave in the Subthermocline Equatorial Pacific

WILLIAM S. KESSLER

NOAA/Pacific Marine Environmental Laboratory, Seattle, Washington

JULIAN P. MCCREARY

Nova University Oceanographic Center, Dania, Florida

(Manuscript received 28 February 1992, in final form 10 August 1992)

ABSTRACT

The annual cycle of temperature in the subthermocline equatorial Pacific is studied using a new compilation of historical hydrographic profiles. The observations have several characteristics suggestive of a vertically propagating, first meridional mode ($l = 1$) long-wavelength Rossby wave: phase lines that slope downward from east to west indicative of upward and westward phase propagation, amplitude maxima parallel to phase lines, and nearly symmetric off-equatorial maxima of annual amplitude. Estimates of zonal wavenumber, vertical wavenumber, and the location of maxima of isotherm displacements are consistent with those of the $l = 1$ Rossby wave.

A solution to a linear continuously stratified model, driven by a version of the observed annual wind field, confirms this interpretation. The solution is dominated by a vertically propagating, $l = 1$ Rossby wave. The wave is generated primarily by the westward-propagating component of the equatorial zonal wind field; it carries energy along WKB ray paths into the deep ocean. Both amplitude and phase of the model density field agree well with the observations. There are, however, two prominent differences between the observations and the solution: first, in the solution a boundary-reflected $l = 3$ Rossby wave is present in the deep eastern Pacific but is apparently absent in the data; second, the model solution is nearly symmetric about the equator, while the observations are symmetric in phase but have larger amplitude in the Northern Hemisphere.

Thus, efficient vertical propagation of Rossby wave energy through the thermocline into the deep ocean appears to be an important oceanic process. The lack of this process in single active-layer models may explain the unrealistically high amplitudes of off-equatorial variability that are produced in them, since such models necessarily trap all energy in the surface layer.

1. Introduction

Lukas and Firing (1985) interpreted an annual signal in hydrographic observations taken during the Hawaii-Tahiti Shuttle Experiment (150°–158°W) as a vertically propagating, equatorially trapped long Rossby wave. They found that the vertical and meridional structure of the observed density variability between 300 and 1000 m in the equatorial waveguide was consistent with the propagation through the region of an annual, first meridional mode ($l = 1$) Rossby wave. Although the Shuttle data formed essentially a single meridional section and a single realization of the annual cycle, Lukas and Firing (1985) suggested that the observed fluctuations could be driven directly by the annual cycle of equatorial winds in the eastern Pacific.

Luyten and Roemmich (1982) analyzed moored velocity measurements below the thermocline in the western Indian Ocean and found energetic semiannual variability of zonal currents, which they interpreted to be a combination of vertically propagating Kelvin and $l = 1$ Rossby waves. They estimated vertical wavelengths of about 5 km and attributed the downward energy flux to direct wind driving. Weisberg and Horigan (1981) studied spectra from an array of subsurface velocity moorings in the Gulf of Guinea. The results could be partly explained by the occurrence of long Rossby waves, but they also argued that nonlinear mechanisms were important. Eriksen (1981) studied deep velocity moorings in the central equatorial Pacific. He found relatively broad, but equatorially trapped, features, which could only be explained as low-frequency, low meridional mode Rossby waves. Their vertical wavelengths were estimated at several hundred meters, and a net downward energy flux was hypothesized. Other studies have reported observations of wind-driven Rossby–gravity waves in the deep equatorial ocean (see, for example, Weisberg et al. 1979). Thus, observations in all the equatorial oceans suggest that low-frequency, vertically propagating equatorially trapped waves are a significant and common source of energy below the equatorial thermocline.

The question of whether wind-driven energy can

Corresponding author address: Dr. William S. Kessler, NOAA/PMEL/OCRD, 7600 Sand Point Way NE, Seattle, WA 98115-0070.

propagate efficiently through the sharp equatorial thermocline has been a subject of controversy in the recent literature. McCreary (1984), using a linear, continuously stratified model, obtained solutions that were dominated by Rossby and Kelvin "beams" approximately following the ray paths expected from simple WKB theory. Using the same model, Rothstein et al. (1985) subsequently showed that the sharp equatorial pycnocline was not necessarily a barrier to the vertical propagation of long Rossby waves. They found that much of the wave energy incident on a realistic pycnocline was transmitted directly through it into the deep ocean; moreover, multiple reflections of wave rays from the pycnocline and surface occurred, which had the net effect that *all* wind-driven energy eventually reached the deep ocean. In contrast, the solutions of Gent and Luyten (1985) suggested that for realistic pycnoclines much of the incident long vertical wavelength energy is reflected, with little energy reaching the deep ocean; in particular, the Gent and Luyten (1985) results indicated that waves of the vertical scale studied here (several kilometers) should have about 90% of their energy trapped above the thermocline. A limitation of the Gent and Luyten (1985) model, however, is that it described a *single* reflection from a sharp density discontinuity. A more complete picture of the process would include the reflected wave rays repeatedly returning to the surface and being reflected back down to the thermocline, each time leaking a small fraction of the wave energy through to the deep ocean. Such *multiple* reflections are clearly visible in the solutions of Rothstein et al. (1985) when the upper layer is assumed to be strongly stratified. Since the upper layer of the equatorial Pacific actually has very weak stratification, ray paths above the thermocline are nearly vertical (see the Appendix), and the multiple reflections occur in a region of small zonal extent. The result of the multiple reflections is to allow much larger total transmissivity than was indicated by the Gent and Luyten (1985) calculation. We return to the question of energy propagation into the deep ocean in section 4.

Gent (1985) forced a linear, continuously stratified model with the observed annual cycle of the zonal winds over the Pacific Ocean and compared his solutions to the Lukas and Firing (1985) observations, addressing a similar problem to that studied here. He reported that the solution reproduced the phase of the observed seasonal cycle but not the amplitude, which was too weak by a factor of about 3. He also found little evidence of vertically propagating waves in his solutions, arguing that the realistic structure of the wind field, thermocline reflections, and vertical mixing all acted effectively to destroy any distinctive pattern associated with vertically propagating waves. This conclusion differs from the one reached in the present paper, and the discrepancy is discussed in section 4.

In the present paper, we first extend the work of Lukas and Firing (1985) by using a compilation of historical hydrographic data to study the annual signal over the width of the Pacific down to 3000 m, so that the average annual cycle of temperature can be observed in zonal sections. The annual cycle is studied because it is possible, through compositing historical hydrographic data, to construct zonal sections of observations of the annual cycle across the width and depth of the entire Pacific, which otherwise would require a prohibitively expensive observational array. Although the annual signal is important in its own right, it is thought that the results presented here will be applicable to other low-frequency wind-driven signals.

The observed annual cycle is then compared with solutions to the linear, continuously stratified model of McCreary (1984), driven by realistic winds. We find that the most prominent feature of the solution is a vertically propagating $l = 1$ Rossby wave and that both the phase and amplitude of the temperature variability associated with this signal compare well with the observations.

The plan of this paper is as follows. Section 2 discusses data processing and the observed annual cycle of temperature in the subthermocline equatorial Pacific. Section 3 shows model results and comparisons to the observations. Section 4 discusses the results in light of simple theory and previous studies. Properties of vertically propagating Rossby waves relevant to the present research are reviewed in the Appendix.

2. Observations

a. Data

The data used consisted of all hydrographic profiles (no XBTs) from the region 10°S–10°N. The data sources were the archives of the National Oceanographic Data Center (NODC), including many old Nansen bottle profiles dating back to the 1920s, as well as profiles obtained during recent programs (EPOCS, WEPOCS, Surtropac, US-PRC program, Jenex). The total number of profiles used in the present study was 20 408, of which 2558 extend deeper than 1500 m. The distribution of observations (Fig. 1) shows that sampling was good in the far eastern Pacific, fairly good west of the date line, but very spotty in the east-central Pacific between 120° and 150°W. Some of the old observations were of poor quality, and extreme outliers were not uncommon in the NODC archive set, requiring extensive hand editing to remove (about 5% of the profiles were rejected). Even the cleaned data presents a very noisy picture, and certainly some erroneous observations remain. Nevertheless, that the annual cycle appears to be quite robust in the processed data indicates that the cleaning was sufficient and the signal was not overwhelmed by noise. We had hoped to use the observed salinity as well in this study, but the salinity sampling was very sparse and appeared to

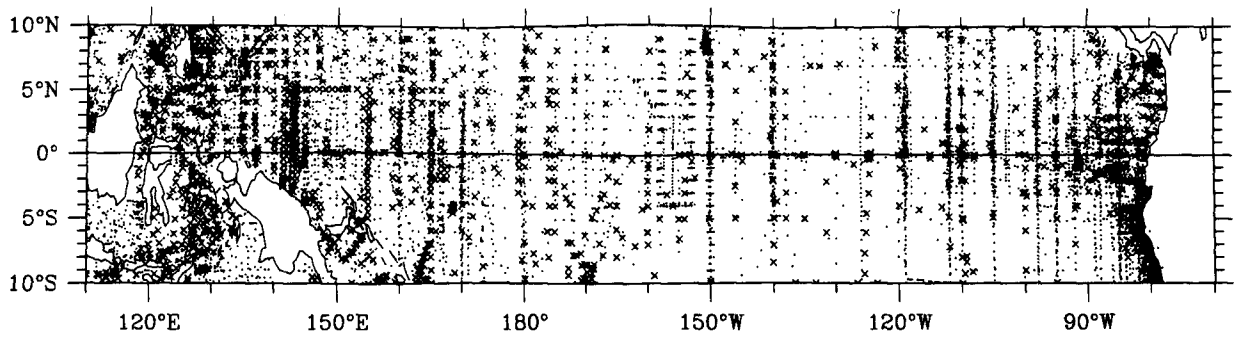

FIG. 1. Location of all hydrographic profiles (CTD and Nansen) studied. A total of 20 408 profiles are shown; × indicates the 2558 profiles extending below 1500 m.

have many errors; therefore, only temperature is studied here.

Our intent in the treatment of the observations was to construct a climatology similar to that of Levitus (1982) but focused on the detection of annual equatorial waves in the Pacific. In fact, the waves discussed in this paper are evident to some degree in the Levitus climatology. The new climatology, however, is superior for the present purpose for several reasons. First, Levitus had data available only through about 1973, due to the long time lag in data archiving. Almost twice as many hydrographic profiles are available at present in the equatorial Pacific, and many of the new data are deep, high-quality CTDs. Second, Levitus (1982) made only a crude annual cycle consisting of four average seasons and extending only to 1500 m. With the additional data, we were able to construct 12 average months extending to 3000 m, giving better spatial and temporal resolution of the annual phase. Finally, Levitus (1982) used an objective mapping procedure with the choice of influence radii dictated by the need to have a single mapping scale for the entire World Ocean. This resulted in structures that were too smooth in the equatorial Pacific where the meridional scales are short. Without this constraint, we were able to grid the observations with anisotropic horizontal mapping scales of 5° long and 1/2° lat, giving good resolution of the short meridional structures of equatorial waves.

The gridding was carried out in two steps. First, the temperature data $T_n(x_n, y_n, z_n, t_n)$ from each profile n were linearly interpolated to standard depths z_0 (every 10 m from the surface to 3000 m), thereby creating a modified dataset $T'_n(x_n, y_n, z_0, t_n)$. This interpolation was performed only when two samples in a profile were within selected vertical distances, which increased from 50 m in the upper 100 to 600 m between 2 and 3 km; otherwise, levels were left blank. No extrapolation was done. The time coordinate t_n refers only to the day of the year, all years being composited to make an average year. Second, in a separate computation at each standard depth z_0, the temperatures T'_n were mapped from the irregular locations (x_n, y_n, t_n) onto a regular grid (x_0, y_0, t_0), with grid spacings of 2° long, 1° lat, and 1 month. Specifically, the value of gridded temperature T'' at each grid point (x_0, y_0, t_0) was estimated by the operation

$$T''(x_0, y_0, t_0) = \frac{\sum_{n=1}^{N_p} T'_n W_n}{\sum_{n=1}^{N_p} W_n}, \quad (1)$$

where N_p is the total number of profiles within the "influence region" of a particular grid point (defined below). The Gaussian weight function W_n is given by

$$W_n(x_n, y_n, t_n) = exp\left\{-\left[\left(\frac{x_n - x_0}{X}\right)^2 + \left(\frac{y_n - y_0}{Y}\right)^2 + \left(\frac{t_n - t_0}{\tau}\right)^2\right]\right\} \quad (2)$$

The mapping scales are $X = 5°$ long, $Y = 1/2°$ lat, and $\tau = 1$ month. This operation is similar to a single iteration of objective mapping as used by Levitus (1982).

Because the weight function W_n has a nonzero value everywhere, in theory every observation should be part of the summation for each grid point. However, since this would involve a tremendous amount of computation [the number of terms in the sums (1) would be the product of the number of profiles times the number of grid points times the number of standard depth levels; that is, about 10^{11} terms], and for most of these the weight function would be vanishingly small, the summations were truncated at the point where the weight function equaled e^{-8}. The area where $W_n > e^{-8}$ (which occurs where the distances from the grid point are less than $2\sqrt{2}$ times the mapping scales X, Y, or τ) defines the influence region of a data point and sets the value of N_p. Thus, for example, a profile more than 1.4° lat from a grid point was not mapped to that grid point, so the tight meridional scales were not aliased by the gridding operation. Visualizing the three-dimensional grid (x_0, y_0, t_0), with data points $T'_n(x_n, y_n, t_n)$ scattered irregularly through it, the mapping operation appears as an ellipsoid moving from grid point to grid point, averaging the data points that fall within the ellipsoid. Each data point falls within the summation for several grid points, weighted according to

distance. In regions of very sparse sampling, a single data point may be the only information for one or several grid points. If no data points fell within the ellipsoid at a grid point, it was left blank.

Having constructed the gridded dataset $T''(x_0, y_0, z_0, t_0)$, an annual harmonic was fit to each spatial grid point that had more than eight months of mapped data (out of a possible 12), resulting in a field of complex numbers $\tilde{T}(x_0, y_0, z_0)$, whose amplitude and phase functions are those of the annual harmonic. The field $\tilde{T}$ represents 60%–70% of the annual variance, with the rest represented in the higher harmonics. Next, $\tilde{T}$ was scaled by dividing it by the mean vertical temperature gradient at that grid point and was smoothed in the zonal and vertical directions with a 1–2–1 smoother to reduce small-scale noise; the scaled complex numbers are referred to here as the vertical isotherm displacement ζ, with harmonic amplitude $|\zeta|$ and phase ϕ. This scaling makes for a clearer display of the variability at widely separated depths and also is more physically realistic, since below the thermocline the annual temperature variations are primarily due to vertical motion of water parcels.

b. Results

Figure 2 shows the amplitude and phase of annual isotherm displacement ζ in a zonal section across the Pacific at 4°N. This latitude is shown, rather than its equatorial counterpart, because Rossby waves have their largest amplitudes off the equator; in fact, below the thermocline the pattern of phase at the equator is similar to that in Fig. 2, but the amplitude is somewhat smaller. The zonal section suggests two physical regimes divided by a line extending roughly from 150°E at 3000 m to the eastern boundary at about 600 m. Above and to the west of this line the phase lines (Fig. 2a) are all approximately parallel, with phase propagating upward and westward. Phase lines in this region tend to have a shallow slope in the thermocline and slope more steeply downward at depth. A linear regression on the horizontal variation of ϕ in this region gives a zonal wavelength λ_x of about 15 000 km. The vertical wavelength λ_z is similarly estimated at about 3900 m. The amplitude $|\zeta|$ (Fig. 2b) has an absolute maximum of 40 m near 120°–130°W in the thermocline, and a region of relative maximum extends downward and westward from this region, roughly paralleling phase lines. Below and to the east of the line (in the deep eastern Pacific) ϕ and $|\zeta|$ are disorganized.

Figure 3 shows $|\zeta|$ and ϕ in a meridional section at 170°E, in the center of the region where the phase lines are sloping steeply downward (Fig. 2). The meridional section shows that the vertical structure of ϕ seen in the zonal section at 4°N (Fig. 2) is typical of all latitudes between about 6°S and 6°N, with phase lines approximately horizontal across the equator and upward phase propagation above about 2 km (Fig. 3a). The amplitude has two relative maxima located between about

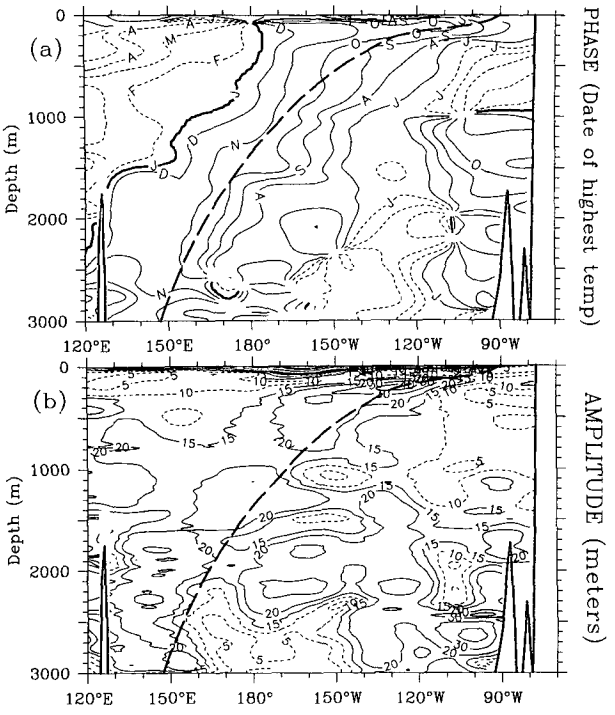

FIG. 2. Zonal section of the annual harmonic of observed vertical isotherm displacement at 4°N. (a) Phase ϕ (date of highest temperature) and (b) amplitude $|\zeta|$ (meters). Phases are labeled in months, with the contour at the first day of each month. The heavy contour is 1 January, then dashed contours are 1 February through 1 June, and line contours are 1 July through 1 December. Heavy lines at the bottom indicate the ocean floor. The heavy dashed line is a WKB ray path of the $l = 1$ Rossby wave in the observed stratification, calculated from Eq. (A6).

2° and 5° north and south of the equator above 1500 m (Fig. 3b). This amplitude structure is similar to the one reported by Lukas and Firing in the region they studied, which was about 4000 km to the east and 1000 m higher in the water column. Lukas and Firing estimated the vertical wavelength to be about 2000 m, about half the value estimated here; however, their estimate was based on observations only of the upper kilometer of the ocean.

To display the variability as a function of x and y together over the whole equatorial Pacific, Fig. 4a shows the depth of the surface where the date of highest temperature (deepest displacement) occurs on 15 October (equivalent to the phase lines marked October in Figs. 2a and 3a). Figure 4b shows $|\zeta|$ on this surface. The surface lies approximately in the center of the large region of parallel phase lines (Fig. 2a) and high amplitude (Fig. 2b). It has a shallow slope in the central Pacific, then plunges steeply downward west of the date line. Additionally, it is roughly symmetric about the equator, with depth contours oriented meridionally, crossing the equator and bending back towards the east at higher latitudes (Fig. 4a). The equatorial minimum and off-equatorial maxima near 5°S and 5°N are clearly seen in the structure of the amplitude $|\zeta|$ on

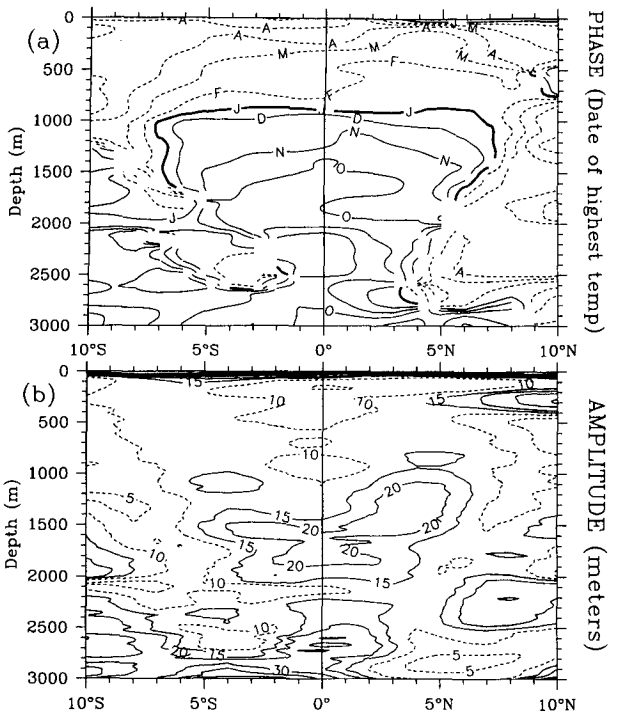

FIG. 3. As in Fig. 2 but for a meridional section at 170°E.

this surface (Fig. 4b). However, although the amplitude pattern is qualitatively symmetric (note the weak but well-defined amplitude maximum at 5°S), $|\zeta|$ is larger in the Northern Hemisphere.

It is possible to check whether the observed signal is consistent with a vertically propagating Rossby wave (see the Appendix). Following Lukas and Firing (1985) and Horigan and Weisberg (1981), we compare estimates of the separation parameter c obtained in three different ways: first, from the Rossby wave dispersion relation using the zonal phase information; second, from the WKB vertical wavenumber using the vertical phase observations; and third, from the meridional structure of the signal. The first method utilizes the dispersion relation (A4) rewritten in the form

$$c = \frac{-\omega(2l+1)}{k} \tag{3}$$

to obtain c. With λ_x estimated to be about 15 000 km, it follows that $k \approx -4.2 \times 10^{-7}$ m^{-1}. Equation (3) then gives $c \approx 1.43$ m s^{-1}, for an annual $l = 1$ Rossby wave. This speed is about midway between the characteristic speeds c_n of the second and third baroclinic modes [Ψ_n in (A1)] of the observed stratification. The second method uses the WKB identity

$$c \equiv \frac{N_b}{|m|} \tag{4}$$

(see the Appendix) to determine c from the vertical phase observations. With λ_z estimated at roughly 3000 m, $m \approx 1.62 \times 10^{-3}$ m^{-1} in a region where N_b averages about 2.2×10^{-3} s^{-1}. According to (4), then, the WKB vertical estimate is $c \approx 1.36$ m s^{-1}, which differs from that obtained from the horizontal wavelength by only about 5%, well below the uncertainty in our estimate of the zonal or vertical wavelengths. Finally, a third estimate for c can be obtained from the location y_m of the off-equatorial maxima in $|\zeta|$ of the $l = 1$ Rossby wave, using the relation

$$c = \frac{2}{3}\beta y_m^2 \tag{5}$$

[see the discussion of (A2) in the Appendix]. With y_m estimated from Fig. 3 to be about 300 km, (5) gives $c \approx 1.37$ m s^{-1}, close to the other two values. (We note, however, that since the estimate depends on the square of the distance y_m, it is highly sensitive to the choice of y_m.) The closeness of all three estimates of c demonstrates that the observed signal is consistent with an $l = 1$ vertically propagating Rossby wave.

Another consistency check arises from the slope of phase lines in Fig. 2. The slope of ray paths in the (x, z) plane for Rossby waves is given by (A6), so that phase propagates upward across a band of energy propagating downward to the west (energy originating at the surface propagates downward to the west). In

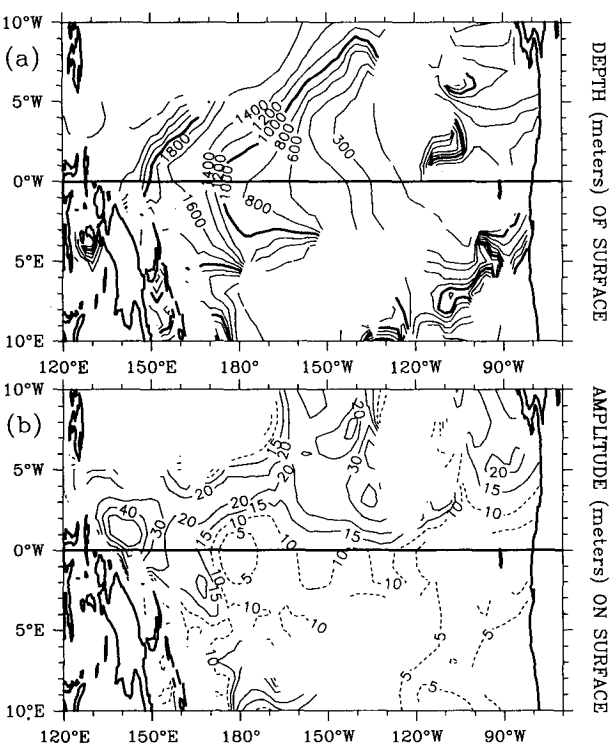

FIG. 4. (a) Depth (m) of the surface where the date of highest temperature of the annual harmonic occurs on 15 October (halfway between the phase isolines October and November in Figs. 2 and 3). (b) Amplitude $|\zeta|$ (m) of the annual harmonic of isotherm displacement on the surface shown in (a).

addition, because the dispersion relation (A5) is nondispersive, phase lines are parallel to WKB ray paths (see the Appendix), and bands of energy descend into the deep ocean parallel to phase lines. The WKB ray path for the $l = 1$ annual Rossby wave obtained from (A6) with the observed mean stratification is plotted in Fig. 2, and the curve is seen to be closely parallel to the phase lines found from the observed temperatures. In particular, note the shallow slope in the thermocline region of large values of N_b and the steeper slope deeper in the water column. For example the ray path that starts at the surface at 90°W follows the October phase contour all the way to 3000 m depth near 150°E. This is a similar but more stringent test than the comparison of characteristic speeds c in the preceding paragraph, since it compares the integral of slope along the ray path rather than a point estimate of wavenumber.

To sum up the description of the annual cycle, the salient results of this section are 1) parallel phase lines, indicative of upward and westward phase propagation; 2) regions of high amplitude off the equator that begin near the surface and bend downward and westward roughly parallel to the phase lines; 3) a region of disorganized phase in the deep eastern Pacific; and 4) consistency with the presence of an $l = 1$ vertically propagating Rossby wave. As we shall see next, the observed signal also closely resembles a solution to a linear, continuously stratified ocean model.

3. A linear, stratified model ocean

In order to obtain a quantitative picture of the linear Rossby waves that can be excited by the annual cycle of Pacific winds, we carried out a series of calculations using the linear, continuously stratified model of McCreary (1980, 1981, 1984). We begin this section by describing the model; it has been thoroughly discussed in the above papers so only a brief summary is given here. Next, the simplification of the wind field that is used to force the model is described. Finally, several solutions are discussed and are then compared with the observations shown in Figs. 2–4.

a. Model description

The equations of motion are linearized about a background state of rest, with the density structure $\rho_b(z)$ and Väisälä frequency $N_b(z)$ [$N_b \equiv -(g/\rho_0)d\rho_b/dz$] taken from the Hawaii–Tahiti Shuttle and other central Pacific observations. The equations are

$$\frac{\partial u}{\partial t} - \beta y v + \frac{1}{\rho_0}\frac{\partial p}{\partial x} = F(x, y, z, t) + \frac{\partial}{\partial z}\left(\nu \frac{\partial u}{\partial z}\right) \quad (6a)$$

$$\frac{\partial v}{\partial t} + \beta y u + \frac{1}{\rho_0}\frac{\partial p}{\partial y} = G(x, y, z, t) + \frac{\partial}{\partial z}\left(\nu \frac{\partial v}{\partial z}\right) \quad (6b)$$

$$\frac{\partial u}{\partial x} + \frac{\partial v}{\partial y} + \frac{\partial w}{\partial z} = 0 \quad (6c)$$

$$\frac{\partial p}{\partial z} = -\rho g \quad (6d)$$

$$\frac{\partial \rho}{\partial t} + w\frac{\partial \rho_b}{\partial z} = \frac{\partial^2}{\partial z^2}(\kappa\rho), \quad (6e)$$

where all variables have their usual definitions. Forcing of the system is by a wind stress that enters the ocean as the zonal and meridional body forces $F(x, y, z, t)$ and $G(x, y, z, t)$, respectively (except for one experiment reported here, G is identically zero). To facilitate comparison with the observations, we also define an additional variable, $\zeta \equiv \rho/(d\rho_b/dz)$, a measure of vertical isopycnal displacement in the model; its amplitude $|\zeta|$ and phase ϕ are then directly comparable to those obtained from the observations.

Surface and bottom boundary conditions are

$$\nu\frac{\partial u}{\partial z} = \nu\frac{\partial v}{\partial z} = w = \kappa\rho = 0 \quad \text{at} \quad z = 0, -D, \quad (7)$$

where D is the depth of the model ocean, which here was taken to be 4500 m. No-stress surface conditions are adopted because the forcing is assumed to be contained entirely in the body forces F and G. The no-stress bottom conditions have little effect on the solutions since large currents are not generated near the ocean bottom. The condition $\kappa\rho = 0$ implies that no SST changes are possible; this limitation has been studied by Rothstein (1984) and is not a major concern here where we are interested in subthermocline variability.

In order that solutions may be represented in an expansion of the vertical normal modes, the body forces must also be separable in z, and we chose the convenient form

$$F(x, y, z, t) = \tau_0 X(x)Y(y)Z(z)e^{-i\omega t}, \quad (8a)$$

where τ_0 is the dimensional amplitude and ω is the (annual) frequency. The zonal structure of the forcing is

$$X(x) = \begin{cases} \sin\left[\dfrac{\pi(x - x_w)}{\Delta x}\right]e^{ikx}, & x_w \leq x \leq x_e \\ 0, & \text{otherwise,} \end{cases} \quad (8b)$$

where x_w and x_e are the western and eastern edges of the wind patch, and $\Delta x = x_e - x_w$. According to (8b), the forcing is confined within a half-sine envelope in x, and inside the envelope it may propagate westward or eastward depending on the sign of k. The meridional structure of the forcing is the Gaussian profile

$$Y(y) = exp\left[-\frac{1}{2}\left(\frac{y - y_0}{\Delta y}\right)^2\right], \quad (8c)$$

which is centered at y_0 and has half-width Δy. The Gaussian profile is useful because it projects easily onto the meridional modes through a simple recursion relation. The vertical structure is

$$Z(z) = \theta(z + H)/H, \tag{8d}$$

where θ is a step function and H is the thickness of the surface layer (where N_b is assumed identically zero). This states that the wind force is distributed uniformly throughout a surface layer of depth H. Here H was taken to be 75 m, but test experiments showed that the results presented are largely insensitive to choices of H less than a few hundred meters.

Two other choices are necessary for the vertical-mode expansion. First, the eddy coefficients must be assumed inversely proportional to N_b^2; that is,

$$\nu = \kappa = \frac{A}{N_b^2}, \tag{9a}$$

where A is a constant. With the value of A chosen (2.3×10^{-4} cm^2 s^{-3}) and the observed N_b^2 profile, ν and κ range from a maximum of about 50 cm^2 s^{-1} in the deep water to a minimum of about 0.5 cm^2 s^{-1} in the center of the thermocline. Equivalently the choice of A sets the damping time for each baroclinic mode. The present value of A gives a damping time of 10 years for the first baroclinic mode; damping times for higher modes decrease by the factor c_1^2/c_n^2. Physically, parameterization (9a) states that vertical friction and mixing are strongest where the stratification is weakest. In the real equatorial ocean, of course, friction and mixing are probably very large only in the high-shear (and high stratification) region near the undercurrent, contrary to (9a). The second necessary choice is the unconventional form of the mixing of heat

$$(\kappa\rho_z)_z \rightarrow (\kappa\rho)_{zz}. \tag{9b}$$

Although the choices (9a) and (9b) are mathematically necessary, the solutions studied here do not depend strongly on friction. We include friction to eliminate inertia–gravity waves associated with very high-order vertical modes, as well as Rossby waves corresponding to high meridional modes that are generated by the reflection of Kelvin waves off the eastern boundary. In fact, the only part of the solution that is sensitive to the value of ν and κ is the reflection from the eastern boundary. Test experiments showed that the directly wind-driven part of the solution (i.e., with no boundaries) was nearly identical when the model was run with no friction ($A = 0$). With an eastern boundary, first-baroclinic-mode damping times from about 2 years to 20 years produced similar solutions to those shown here. Thus, a more realistic parameterization of vertical mixing than (9a) and (9b) is not crucial to this study. (See McCreary 1981, 1984; McPhaden 1981 for further discussion of the sensitivity of solutions to various forms of vertical mixing.)

The ocean basin is unbounded meridionally, but can include north–south barriers to represent eastern and western boundaries. Most of the solutions discussed in section 3c have an eastern boundary only, the sole exception being one solution in an unbounded basin reported in section 3c(2). We neglected the western boundary for two reasons. The first is that no meridionally oriented north–south barrier can accurately represent the coast of New Guinea, Indonesia, and the Philippines; for example, the zonal separation of at least 2500 km between the Philippines and New Guinea will certainly alter the phases of the equatorial reflections due to incoming Rossby waves, a process that the present model cannot simulate. The second is that test experiments showed that when a western boundary was included there was only a small effect on the solution more than a few degrees off the equator; this lack of sensitivity occurred because the western boundary–reflected Kelvin waves are highly trapped to the equator. Due to the Kelvin waves, however, the solutions on the equator differ considerably if western boundary reflections are involved. Since the model western boundary is significantly unrealistic and since we are studying Rossby waves, which have their largest amplitude off the equator, it seemed best to eliminate the western boundary reflections from the solutions altogether. As discussed in section 4, the lack of the western boundary in the solutions presented here is the principal difference between our results and the solutions of Gent (1985).

With boundary conditions (7) and the restrictions specified in Eqs. (8) and (9), the system (6) is separable in x, y, and z, and solutions can be obtained analytically. Solutions are represented as a double sum over N vertical normal modes (the baroclinic modes) and over L meridional modes of equatorially trapped waves [see the discussion of Eq. (A1)]. For the solutions shown in section 3c, $N = 50$ vertical modes and $L = 100$ meridional modes were summed. As indicated in (A1), the double sum can be summed over the vertical modes to produce components composed of waves of only a particular type l. For this reason, when $l \geq 1$, we refer to q_l as the lth Rossby wave of the solution.

b. *The wind field*

No fundamental difficulty exists in solving Eq. (6) numerically using the observed winds. In order to utilize the preceding analytic model, we sought to represent the forcing as a sum of several components, each having the form (8). Because the model is linear, the complete solution is then the superposition of the individual solutions forced by each wind component. This simplification is also useful in that the particular features in the wind most responsible for generating the oceanic signals can be isolated; moreover, it filters much of the small-scale noise out of the observed wind field.

Figure 5 shows the annual harmonic of zonal wind stress from the Florida State University (FSU) wind product, averaged over the years 1961–87. The strongest annual signal is the out-of-phase oscillation of the trades. Between 5° and 10° from the equator, the an-

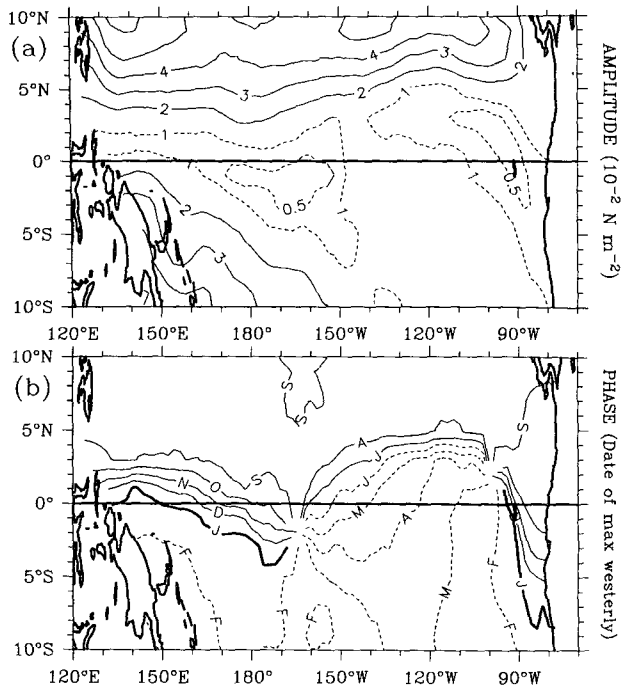

FIG. 5. The annual harmonic of observed zonal wind stress, averaged over 1961 through 1987 from the Florida State University wind product. (a) Amplitude (10^{-2} N m^{-2}) and (b) phase (date of maximum westerly). Phase contouring convention as in Fig. 2.

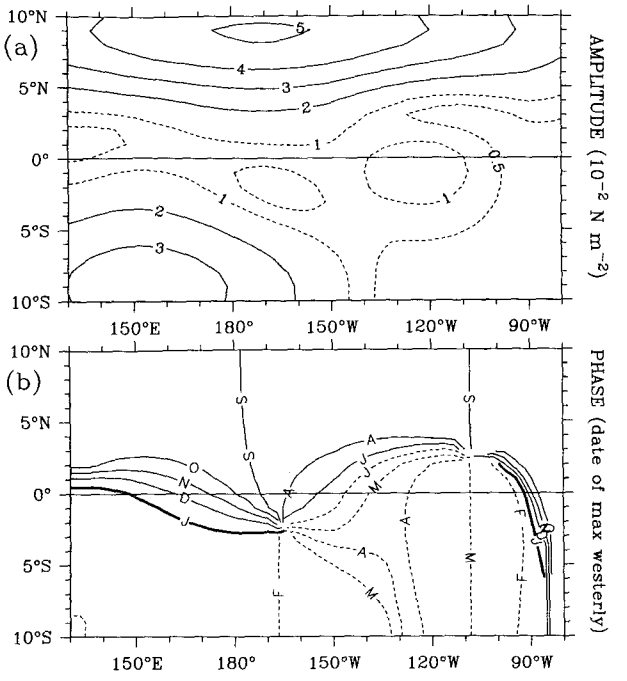

FIG. 6. The annual harmonic of idealized zonal wind stress used to force the model ocean. (a) Amplitude (10^{-2} N m^{-2}) and (b) phase (date of maximum westerly). The field results from the sum of the four functions shown in Fig. 7, which are defined by (8) with values given in Table 1. This idealized wind field is directly comparable to the observed winds shown in Fig. 5. Phase contouring convention as in Fig. 2.

nual harmonic has very little phase variation across the basin, with strongest westerlies (weakest trades) in August–September in the north and February–March in the south. On the equator, there is a nearly linear propagation of the annual wind signal from east to west, taking slightly more than one year to cross the basin (Fig. 5b), as has been pointed out by Meyers (1979), Lukas and Firing (1985), and Gent (1985). The equator is a minimum in annual cycle amplitude (Fig. 5a).

Our simplification of the wind field (Fig. 6) was developed by trial and experiment, seeking analytic components that would characterize the large-scale features of the annual cycle of the winds. We found that an accurate representation could be obtained with only four components. Table 1 gives the defining parameters, and Fig. 7 shows the four functions schematically. The two off-equatorial functions (representing the ITCZ and SPCZ) are stationary in x; that is, $k = 0$ in (8b), whereas the main equatorial field PG propagates westward ($k = 2\pi/\Delta x$; see Table 1). A small stationary equatorial piece (EP) in the eastern Pacific is added so the wind attains the observed amplitude maximum near 120°W (Fig. 5a). The sum of these four functions gives a wind field that captures the large-scale features of the observed winds (compare Figs. 5 and 6). The difference field between the observed and simplified wind fields (not shown) demonstrates that the amplitude of the difference is small and the phase difference has only small-scale structure, indicating that the simplification represents most of the large-scale features of the annual wind forcing.

c. *Solutions*

In the first part of this section, we discuss the "main run" of our model, that is, the solution forced by the complete wind field shown in Fig. 6 in a basin with an eastern boundary. In the second part, several test calculations designed to isolate the processes that cause the dominant features of the main run are reported.

1) THE MAIN RUN

Figure 8 shows $|\zeta|$ and ϕ in a zonal section at 4°N, directly comparable to the observed section shown in Fig. 2. (Although the model ocean has a depth of 4500 m, only the upper 3000 m are shown to facilitate the comparison.) Both phase and amplitude are similar to the observations, except in the deep eastern Pacific. Phase lines in the central and western ocean (Fig. 8a) have a shallow slope in the thermocline, then plunge steeply downward, roughly parallel to the WKB ray paths for an $l = 1$ Rossby wave (Fig. 2), and phase differences between the observations and the solution are generally one month or less. A region of high am-

TABLE 1. Parameters that define the idealized wind fields. Four wind fields, each of the form (8) were used to force the model (Fig. 7). For convenience, these are named ITCZ (field centered at 9°N), SPCZ (field centered at 9°S), PG (westward-progagating field on the equator), and EP (small equatorial piece at 120°W). The table below shows the value of the parameters used to define each of these wind fields.

	τ_0 (10^{-2} N m^{-2})	ϕ	x_w	x_e	k	y_0 (km)	Δy (km)	H (m)
ITCZ	5	Sep	60°E	40°W	0	1000	400	75
SPCZ	3.5	Feb	80°E	130°W	0	−1000	550	75
PG	1	Jan	135°E	85°W	$2\pi/\Delta x$	0	500	75
EP	0.75	Mar	150°W	90°W	0	0	400	75

plitude extends from near the surface in the east-central Pacific downward and westward to the western boundary near 2–3-km depth (Fig. 8b). The zonal wavelength, estimated as the gradient of the phase, is about 15 000 km, the same as in the observations. This indicates that this part of the solution is forced predominantly by the westward-propagating component of the wind stress (PG in Table 1), which also has a zonal wavelength of about 15 500 km, and this is confirmed in section 3c(2).

In the deep far eastern Pacific, there is a band of high amplitude extending from the eastern boundary at a depth of about 500 m to 100°W at 3000 m. This feature is one of the significant differences between the solution and the observations. This band is roughly parallel to the ray path of the $l = 3$ Rossby wave that reflects from the eastern boundary [see Eq. (A6) and the dashed line on Fig. 8]. This good agreement indicates that the $l = 3$ wave accounts for most of the energy in this part of the solution.

Bottom reflection also makes a contribution to the solution. Upward bumps are seen in the solution phase lines along the upward ray paths of both the $l = 1$ and $l = 3$ Rossby waves in Fig. 8a, and these are associated with minima of amplitude (Fig. 8b). These wave rays have reflected off the eastern boundary, then off the bottom, and destructively interfere with the main downward-propagating $l = 1$ wave. Similar bumps are found in the observed zonal phase section (Fig. 2a), although these may be just observational noise.

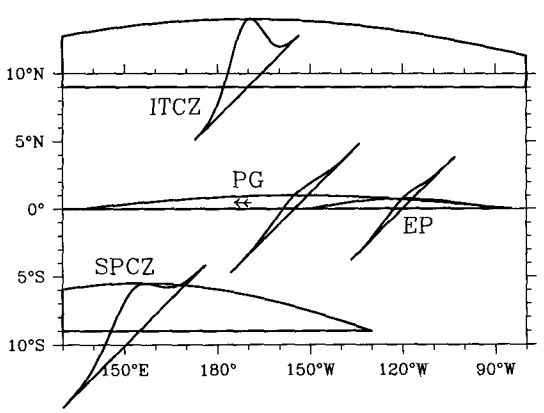

FIG. 7. Schematic of the four functions used to idealize the annual cycle of the wind. Each of the functions has the form (8), with values given in Table 1. The horizontal baseline of each function shows its central latitude (y_0), the upper curve shows the zonal shape of the envelope (all are half-sines within the model ocean limits), and the height shows the relative amplitude. All have a Gaussian shape in the meridional direction, with parameters given in Table 1. The length of the slanted baseline is proportional to the meridional e-folding scale of the Gaussian (Δy). For convenience, the functions are named ITCZ, centered at $y_0 = 1000$ km (9°N); SPCZ, centered at $y_0 = -1000$ km (9°S); PG, centered on the equator and propagating westward (shown by arrow); and EP, centered on the equator and stationary near 120°W. The annual harmonic of the sum of the four functions is shown in Fig. 6.

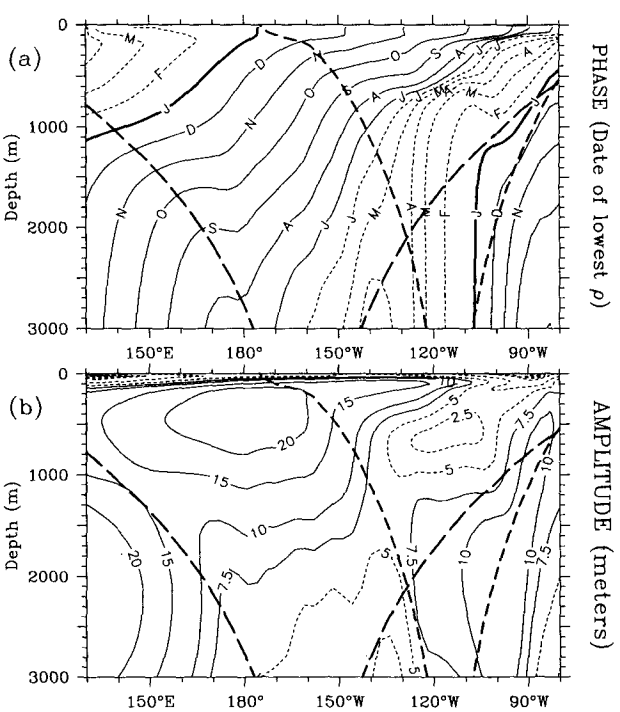

FIG. 8. The annual harmonic of vertical isopycnal displacement ζ at 4°N, from the model solution forced by the winds shown in Fig. 6 (the "main run"). (a) Phase ϕ (date of lowest density) and (b) amplitude $|\zeta|$ (meters). Phase contouring convention as in Fig. 2. The heavy dashed lines are ray paths of the $l = 1$ (long dashes) and $l = 3$ (short dashes) Rossby waves in the observed stratification. Both ray paths are shown reflecting from the eastern boundary at a depth of 600 m, then off the bottom. This solution is directly comparable to the observed isotherm displacements shown in Fig. 2.

Figure 9 shows $|\zeta|$ and ϕ on a meridional section at 170°E, directly comparable to the observed section (Fig. 3). The phase pattern (Fig. 9a) has an equatorially trapped structure similar to the observations, with phase lines roughly horizontal across the equator, but the solution phases are displaced somewhat higher in the water column than in the observed section. The amplitude $|\zeta|$ (Fig. 9b) has nearly symmetric off-equatorial maxima, and these maxima extend over a larger vertical extent than do the observed maxima, with 20-m amplitudes seen up to almost 300-m depth. In the observed section (Fig. 3b), the maxima are concentrated near 1000 m to 1500 m depth and are only weakly present higher in the water column.

Figure 10 shows the depth of the surface where the date of lowest density in the model solution occurs on 15 October, directly comparable to Fig. 4 for the observations. As in the observations, the model October constant phase surface occurs approximately in the center of the amplitude maximum at 4° (Fig. 8). Also in agreement with the observations, the depth contours cross the equator and bend back towards the east beginning at about 3°–4° latitude. Equation (A6) shows that the slope of long Rossby wave ray paths increases with l, so their energy descends into the deep ocean more rapidly. Since the meridional structures of waves with higher l extend to higher latitudes, the net effect is to produce the striking backward bending of the depth patterns seen in Figs. 4 and 10. The amplitude

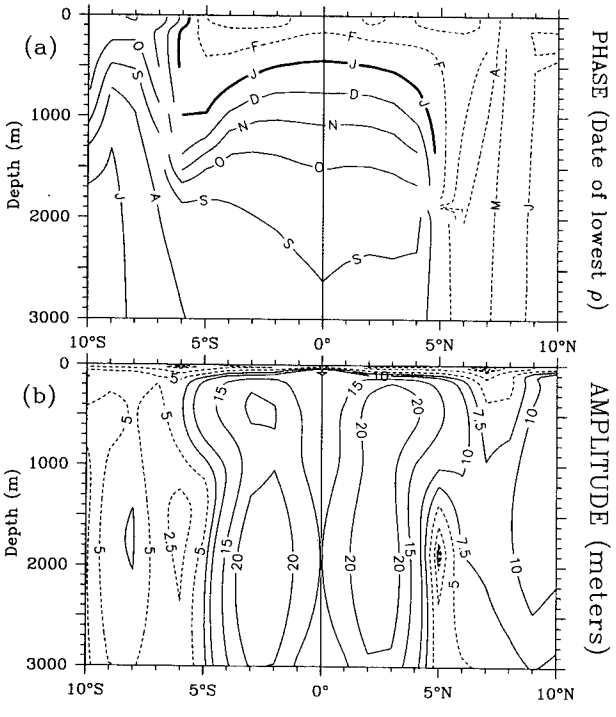

FIG. 9. As in Fig. 8 but a meridional section at 170°E. This solution is directly comparable to the observed isotherm displacements shown in Fig. 3.

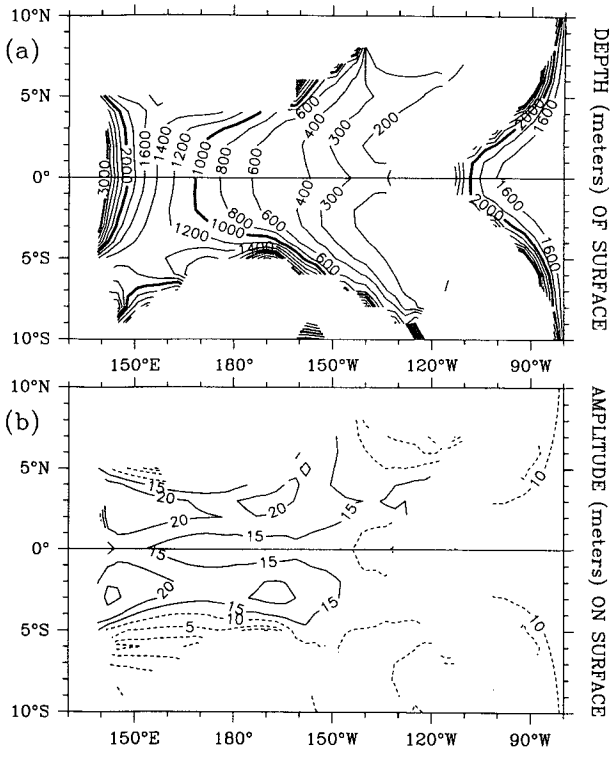

FIG. 10. (a) Depth (m) of the surface where the date of lowest density of the annual harmonic in the model solution ("main run") occurs on 15 October (halfway between the phase lines October and November in Fig. 8), and (b) the amplitude $|\zeta|$ (m) of the annual harmonic of isopycnal displacement on the surface shown in (a). This solution is directly comparable to the observed isotherm displacements shown in Fig. 4.

$|\zeta|$ on the constant phase surface shows an equatorial minimum and off-equatorial maxima (Fig. 10b). Comparison with Fig. 4 reveals a second important difference between the model solution and the observations: the model solution is nearly (but not perfectly) symmetric, while the observations are qualitatively symmetric but have much larger amplitude in the Northern Hemisphere.

2) OTHER SOLUTIONS

A useful feature of the analytic model is that solutions can readily be separated into their component waves. Figure 11 shows the contribution of just the $l = 1$ Rossby wave to the solutions at 4°N. Everywhere but in the deep far eastern Pacific, the $l = 1$ wave is very similar to the complete solution, demonstrating that it is the dominant signal at this latitude. Most of the $l = 1$ wave is directly forced by winds over the interior ocean, but its far eastern part is generated indirectly by the reflection of wind-generated Kelvin waves from the eastern boundary (see the discussion of Fig. 14 below). Note that the deep eastern Pacific is a shadow zone for this wave.

What components of the wind field account for the

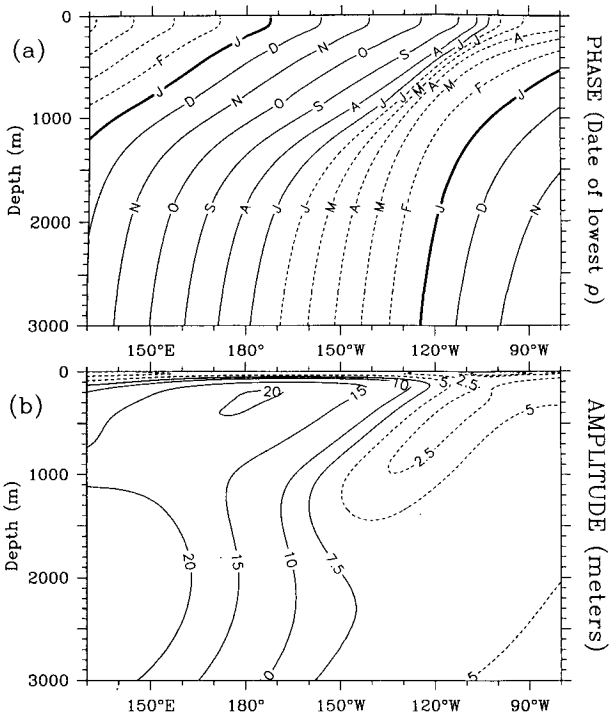

FIG. 11. As in Fig. 8 but for the first meridional mode ($l = 1$) part of the solution only.

dominant features in the solution? To answer this question, we carried out four test calculations forced by the individual wind patches shown in Fig. 7. The responses to the ITCZ and SPCZ did not resemble the main run at all and were much weaker in amplitude. Figure 12 shows $|\zeta|$ and ϕ at 4°N when the model is forced only with the westward-propagating part of the idealized wind field, PG (see Table 1). In the western half of the basin this partial solution is in some ways closer to the observed phase pattern (Fig. 2a) than is the complete solution (Fig. 8a). Many aspects of this solution are also similar to the solution when the model is forced with all four wind components. In contrast to the main run, the amplitude maximum seen in the deep eastern Pacific with full four-component forcing is now absent; this difference occurs because westward-propagating forcing projects weakly onto the Kelvin wave (Wunsch 1977; Weisberg and Tang 1983); it is this wave incident on the eastern boundary that excites significant Rossby wave reflections. If this wind component were not westward propagating, large-amplitude Kelvin waves would be produced, and eastern boundary reflection of these would be an important pathway for energy entering the subthermocline ocean. To check this conclusion, the calculation shown in Fig. 12 was repeated, but with stationary forcing [that is, forcing parameters PG (see Table 1) with $k = 0$]; Figure 13 shows $|\zeta|$ and ϕ for this solution. In this case, the reflected waves form a major part of the amplitude, which is considerably larger than when the forcing propagates. Note how much stronger the $l = 3$ reflected wave is now in relation to the directly wind-forced $l = 1$ wave. The structure of the model response to the wind patch EP (see Table 1 and Fig. 7) closely resembles that in Fig. 13, and so is not shown. The major difference from Fig. 13 is its amplitude, which is smaller by about a factor of 3 because of the considerably shorter zonal extent of the EP patch. Nevertheless, the EP patch, like the solution shown in Fig. 13 but unlike any of the other forcing functions, does produce a significant Kelvin wave and consequent eastern boundary–reflected Rossby waves. It is the EP component of the solution, then, that accounts for much of the reflected $l = 3$ Rossby wave signal present in the complete solution.

Figure 14 shows the solution at 4°N forced by the same four wind components but in this case without an eastern boundary. Everywhere above 2-km depth and west of about 150°W this solution is nearly identical to the solution with an eastern boundary (Fig. 8). Clearly the major features of the main run are directly driven by the winds over the interior ocean; boundary reflection plays a relatively minor role except in specific regions. In particular, the band of high amplitude in the deep eastern ocean is absent, indicating that this feature is due entirely to reflection. Also, the phase pattern in the shallow eastern Pacific shows that the packed phase lines in the full solution in this region are a reflected signal.

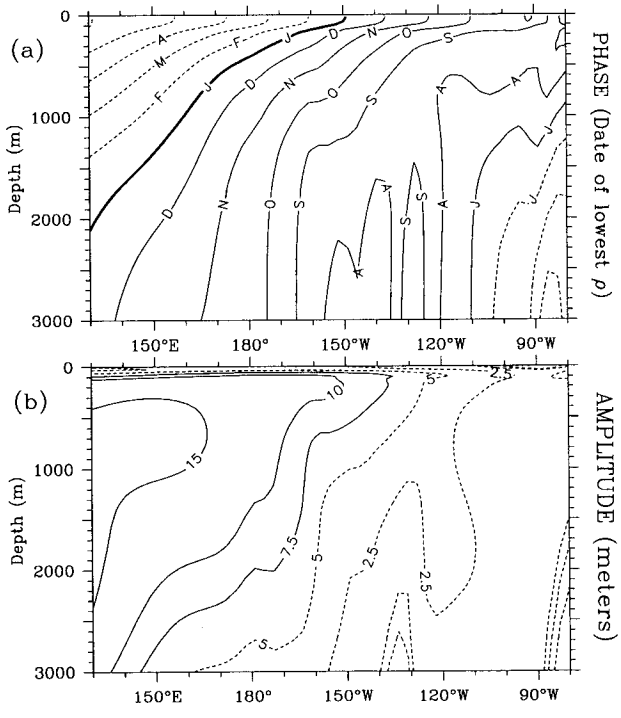

FIG. 12. As in Fig. 8 but for the solution forced with the westward-propagating part of the idealized winds only (parameters PG in Table 1).

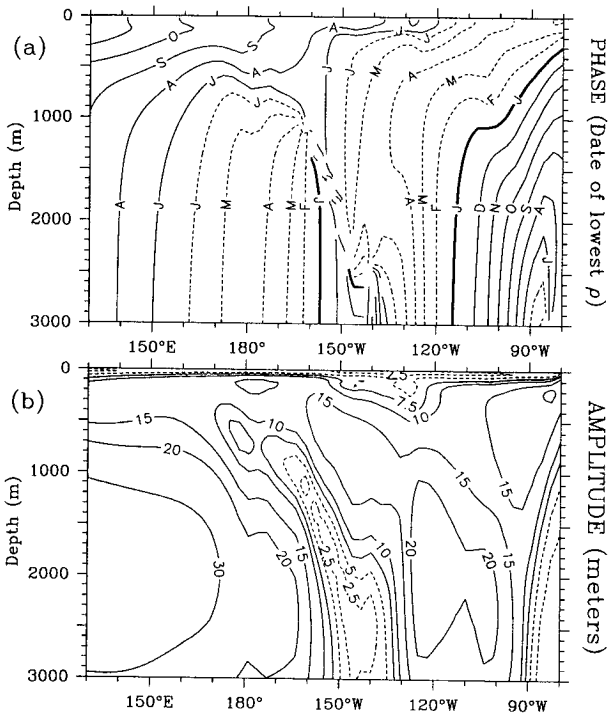

FIG. 13. As in Fig. 12 but for stationary, rather than propagating, wind forcing. Parameters are all the same as PG in Table 1 except that $k = 0$ rather than $2\pi/\Delta x$.

Lukas and Firing (1985) attributed the asymmetry about the equator in the observed annual cycle amplitudes either to asymmetric zonal wind forcing by the ITCZ or to the annual cycle of cross-equatorial winds in the eastern Pacific. The lack of asymmetry in the main run, as well as the weak response to the ITCZ patch, suggests that the asymmetry of the ITCZ is, in fact, not the cause. To test their second hypothesis, we performed an experiment forcing the model with a meridional wind stress [$G \neq 0$ in Eq. (6b)] of roughly the same form as observed (not shown). Although the amplitude of annual meridional stress variability is about the same size or slightly larger than that of the zonal stress in the equatorial eastern Pacific, the amplitude of the solution (not shown) was about an order of magnitude smaller. [Indeed, meridional winds are expected from theoretical considerations to force low-frequency waves more weakly than zonal winds. For example, forcing of the v equation by an x-independent meridional wind stress is proportional to the frequency (Moore and Philander 1977).] Thus, meridional winds also appear unlikely to be the cause of the observed asymmetry.

4. Discussion

With the exception of two significant differences, the observed annual cycle of temperature in the subthermocline equatorial Pacific is closely matched by a solution to a linear, continuously stratified model forced by a simplified, but accurate, version of the observed winds. The most prominent feature in both the observations and the solution is a wide band of energy that slopes downward from the thermocline in the east-central Pacific into the deep western Pacific. The observations suggest and the model demonstrates that this signal is an $l = 1$ vertically propagating Rossby wave directly forced by the wind, confirming the hypothesis of Lukas and Firing (1985). The important differences are 1) the model solution in the deep far eastern Pacific is dominated by an $l = 3$ Rossby wave reflected from the eastern boundary, while the observed annual cycle in this region is disorganized and not clearly associated with large-scale wave processes and 2) the solution is nearly symmetric about the equator, while the observations have similar phase about the equator but larger amplitude in the Northern Hemisphere.

The far eastern Pacific is one of the most densely sampled regions (Fig. 1), so the first discrepancy is probably not due to sampling problems. The coastline of South America is not a straight north–south boundary as it is in the model, so it may be that boundary reflections in the ocean produce interference patterns that result in the apparently disorganized phases observed (Fig. 2a). Unfortunately, this speculation cannot be confirmed using the present model, which requires straight north–south boundaries, and the reason for the difference remains unknown. However, the disor-

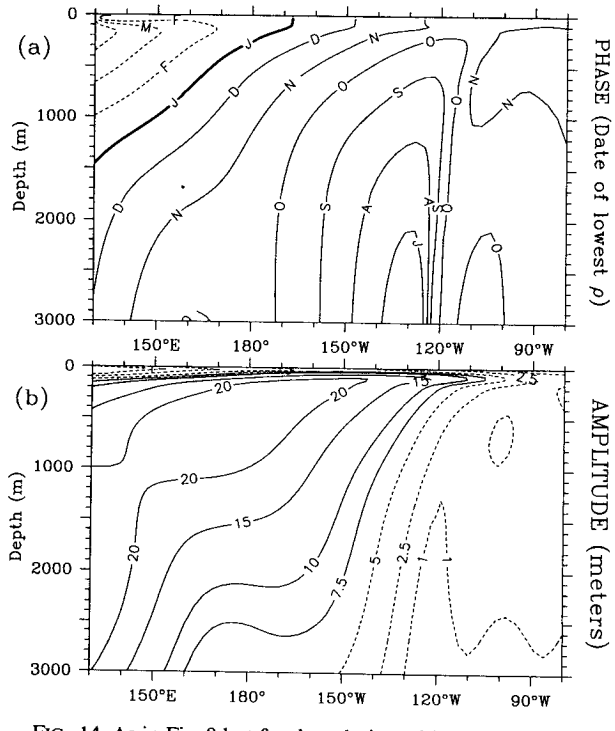

FIG. 14. As in Fig. 8 but for the solution with no boundaries.

ganized phase pattern in the deep far eastern Pacific is consistent with this region being a shadow zone for the dominant $l = 1$ Rossby wave.

The second discrepancy, in which the observations are not nearly as symmetric about the equator as the solution, might be partly due to the very sparse sampling in the central Pacific (Fig. 1). However, Lukas and Firing (1985) noted the same asymmetry in the Hawaii–Tahiti Shuttle temperatures (which were relatively well sampled), so the poor sampling is not likely to provide a complete explanation. As discussed in section 3c(2), neither asymmetric zonal winds nor the annual cycle of cross-equatorial winds are likely to be the cause of the observed asymmetry in the ocean variability. We note a significant asymmetry in the oceanic environment in the east-central Pacific where the major signal propagates through the thermocline (Fig. 2). The thermocline north of the equator is extremely tight, with less than 100 m between 12° and 26°C at 5°N in the central Pacific; by contrast, at 5°S the vertical separation is about 150 m (Kessler and Taft 1987). The 20°C isotherm, which is often used to define the center of the thermocline, is found at about 145 m at 5°N but at about 190 m at 5°S (Kessler and Taft 1987). In addition, the zonal current structure is asymmetric, with the westward South Equatorial Current extending across the equator to 2°–3°N and the eastward North Equatorial Countercurrent stretching from about 3° to 10°N. The linear model used in the present work cannot be used to study the effects of these asymmetries because it requires separability of the vertical and horizontal mean structures; N_b^2 is assumed to be a function of z alone, and there can be no mean currents. It is unclear how the structure of the meridional wave modes would change in an ocean where the mean density field is asymmetric in y. At the present time, the reason for the observed asymmetry in the observations remains unknown.

The predictions of ray theory are generally confirmed in exact solutions to Eq. (6) (see McCreary 1984). On the other hand, ray theory involves approximations that can sometimes fail. For example, as noted in the Introduction, if there is a sharp thermocline, energy will *reflect* from, as well as transmit through, the thermocline. A more severe breakdown of ray theory can occur when the background currents are large. McPhaden et al. (1986) have shown that a vertically propagating Kelvin wave can be almost entirely absorbed by critical surfaces (where the phase speed of the wave is equal to the speed of the background current). Similarly, Proehl (1990) has shown that vertically propagating Rossby waves are distorted, but not absorbed, by critical surfaces. Thus, the existence of near-surface currents is expected to modify the downward propagation of energy considerably. The absorption of Kelvin waves at critical surfaces may provide another explanation for why the reflected Rossby waves seen in the model solution are apparently absent from the observations: some of the Kelvin wave energy in the ocean may be absorbed by the mean equatorial undercurrent before it reaches the eastern boundary.

In spite of these limitations, ray theory should still be valid below the thermocline, where the stratification and currents are weak. In this regard, we note that the observed phase lines at 4°N (Fig. 2a) do not begin at the surface and trend downward, as do the WKB ray paths (Fig. 2) or the phase lines in the model solution (Fig. 8a); instead, the observed phase pattern shows a sharp vertical gradient of phase between the surface and the midthermocline, and the phase lines seen at depth begin their downward propagation from the thermocline itself (Fig. 2a). This property suggests that the deep ocean is forced directly by vertical movements of the thermocline, which in turn result from convergences and divergences in the upper layer induced by variations in the surface wind stress. Then the question raised by Gent and Luyten (1985) and Rothstein et al. (1985) of how wave rays are reflected and distorted in the complex flow field of the upper equatorial ocean is moot, and a more useful description is of a thick layer of fluid with only slow variations in stratification (the subthermocline ocean) being forced by a large-scale distribution of vertical velocity at its upper boundary (the base of the thermocline). Although the details of the dynamics in the mixed layer are poorly understood, many simple models have been able to reproduce the low-frequency wind-driven vertical displacements fairly accurately. In the weakly varying subthermocline ocean, the WKB description is appropriate, and our results showing close correspondence between WKB wave rays and our observations are not surprising. Any model that realistically simulates low-frequency variations in upper-layer thickness should be a good tool for predicting the response of the deep ocean to the winds. The thermocline motions should simply propagate downwards and westwards along the wave rays defined by (A6), with the energy partitioned among meridional mode numbers l according to the meridional structure of the forcing.

It was noted in section 3c(1) that the bending back of depth contours seen in Figs. 4 and 10 could be due to the increase in steepness of the slope of long Rossby wave ray paths with increasing l, so off-equatorial signals descend into the deep ocean quite rapidly [see the discussion of (A6)]. This same property may also account for the unrealistically high amplitude of off-equatorial Rossby waves seen in single-active-layer reduced gravity models (Kubota and O'Brien 1988; Kessler 1990, 1991). Kessler (1991) noted that the interannual variability of upper-layer thickness in the FSU linear reduced gravity model had correct amplitude near the equator, but the model variability became increasingly exaggerated compared to observations as the latitude increased, being a factor of 4 or 5 too large by 15°N [compare Fig. 3a of Kubota and O'Brien (1988) with Fig. 4 of Kessler (1991)]. Additionally,

Kessler (1990) found that Rossby waves observed to be reflecting off the American coast at 10°–15°N following El Niño events apparently disappeared from the upper ocean within a few thousand kilometers, although an inviscid single-active-layer model showed these signals radiating across the whole ocean. Kessler (1990) found that a three-year damping time gave the most realistic simulation; in light of the present results, this damping was apparently a crude way to model vertical propagation in a single-active-layer model. In the continuously stratified ocean, waves off the equator rapidly propagate into the subthermocline ocean, and their amplitude is lost from the upper layer. Single-active-layer models preclude vertical propagation, essentially trapping wave energy in the upper layer, leading to unrealistically large amplitudes, particularly at higher latitudes. Vertical propagation of wave rays, present in the ocean but absent from the single-active-layer models, is a consistent explanation for these discrepancies. Although a single baroclinic mode may produce an incorrect picture of the wave-induced variability in the tropical Pacific, we note that only a few modes can be sufficient to show vertical propagation as observed. The solutions presented here were constructed by summing over 50 baroclinic modes, but very similar results were obtained by summing over as few as five modes.

As noted in the Introduction, Gent (1985) addressed the same theoretical problem that we have but reported no evidence of coherent, vertically propagating waves below the thermocline in his solutions driven by realistic winds. There are several dynamical differences between his model and ours that might account for the discrepancy. First, his model assumed the long-wave approximation, while ours does not. Second, his forcing was the Hellerman and Rosenstein (1983) annual cycle of the winds, whereas our forcing is an idealized annual cycle of the FSU winds. Third, values of the parameterization of vertical mixing used in his model differ slightly from ours, but this is not likely to be an important distinction since our solutions are only weakly dependent on the strength of mixing (section 3a). [Gent (1985) pointed out that a prominent $l = 1$ Rossby wave in a test solution in which strong winds extended to the eastern boundary was significantly damped by vertical mixing (compare his Figs. 10c and 10d). We duplicated this solution and found that this wave was generated by the reflection of wind-forced surface currents (the Yoshida jet) at the eastern boundary; hence, it had a small vertical scale of a few hundred meters, similar to the "beams" shown by McCreary (1984), and was easily damped by friction. In contrast, the Rossby wave in the observations and our solutions is generated directly by winds in the interior ocean and has a vertical scale of several kilometers and, therefore, is not strongly affected by mixing.] Finally, all of his solutions were obtained in a basin with a meridionally oriented western boundary, whereas the present model was run with an open western boundary (section 3a). We carried out a series of test experiments in which a western boundary (at 130°E) was included in our model (the forcing and all model parameters were otherwise exactly as in our "main run" described in section 3a) and found that the solutions were nearly identical to the ones reported by Gent (1985); moreover, the $l = 1$ Rossby wave was still clearly visible in these tests. Thus, dynamical differences between the models cannot explain the divergent conclusions in the two studies.

It follows that the divergent conclusions arise primarily from a difference in interpretation. [In support of this idea, we note that the $l = 1$ Rossby wave does appear to be present in Gent's (1985) Fig. 9, driven by realistic winds. This meridional section clearly displays amplitude maxima at about 3°–4°N, minima on the equator, and weaker maxima near 3°–4°S, in good agreement with our results and with an interpretation in terms of an $l = 1$ Rossby wave. The figure also shows that this signal is not greatly influenced by the type of vertical mixing used, consistent with the fact that our solutions are not sensitive to mixing strength.] We think there are two reasons why Gent (1985) did not detect the vertically propagating Rossby wave in his solutions. First, he focused attention on the structure of his solutions along *equatorial* sections. Since Rossby waves have an amplitude minimum at the equator, and the amplitude of western boundary–reflected Kelvin waves are a maximum there, it is more difficult to isolate the Rossby wave contribution. Second, vertical propagation is not as clear in his figures because the variable displayed is either temperature or density, fields that necessarily have their maximum amplitude in the thermocline; in contrast, we work with isopycnal displacement, which has a more uniform distribution of amplitude with depth, emphasizing the vertical propagation. To summarize, we think the divergent conclusions in the two studies result from our isolating as much as possible the $l = 1$ Rossby wave (by omitting the western boundary reflections, examining the region off the equator, and studying vertical isopycnal displacement rather than temperature or density), and not from the relatively minor differences between the model dynamics, wind forcing used, or strength of friction.

This study has provided further evidence that the vertical propagation of Rossby wave energy is an important process in the equatorial Pacific. It also suggests the need for additional work. For example, to investigate the reasons for the observed asymmetry in the $l = 1$ wave, modifications to the linear solutions resulting from mean currents and shears should be determined using a more sophisticated ocean model. Likewise, to examine why the $l = 3$ wave seen in the model solutions is absent in the eastern Pacific, it would be desirable to analyze a model that allows a more realistic boundary than a straight, north–south coastline; moreover,

the effects of a western boundary could be explored in such a model. Finally, it may be possible to construct a composite quasi-periodic ENSO event from the present set of hydrographic data, in the manner of Rasmusson and Carpenter (1982), to observe the vertical propagation of ENSO-driven signals.

Acknowledgments. We thank Jim O'Brien for providing the FSU/TOGA historical wind product; John Toole for the US-PRC hydrographic data; Joel Picaut for the Surtropac data; Eric Firing for the WEPOCS data; and Stan Hayes for the EPOCS data. Stimulating discussions with Dave Chapman, Peter Gent, Roger Lukas, Mike McPhaden, Dennis Moore, and Lew Rothstein helped clarify our ideas. Support for this work was provided by the National Science Foundation under grants OCE-90-12508 (WSK) and OCE-89-12015 (JPM). WSK gratefully acknowledges the opportunity to spend a postdoctoral appointment in the Physical Oceanography Department at the Woods Hole Oceanographic Institution, where much of this work was undertaken.

APPENDIX

Vertically Propagating Equatorial Rossby Waves

Solutions to the model are represented as a double summation of equatorially trapped waves. Let q be any of the model variables u, v, w, p, or ρ in Eq. (6). Then solutions have the form

$$q(x,y,z,t) = \sum_{l=-1}^{L} \left[\sum_{n=1}^{N} q_{nl}(x,\omega)\Phi_{nl}(\eta,\omega)\Psi_n(z)e^{-i\omega t} \right] \equiv \sum_{l=-1}^{L} q_l(x,y,z,t), \tag{A1}$$

where L is the number of meridional wave modes; N the number of baroclinic modes used in the solution; $\Psi_n(z)$ the vertical structure of the wave; $\Phi_{nl}(\eta, \omega)$ its meridional structure, $\eta = (\beta/c_n)^{1/2}y$; and c_n the characteristic speed of the nth vertical mode (see McCreary 1984). The structure functions Ψ and Φ differ for each variable. For example, for the v field, Ψ_n is the nth baroclinic mode ψ_n, and Φ_{nl} is the Hermite function φ_l; for the ρ field, Ψ_n is $\partial\psi_n/\partial z$, and Φ_{nl} is a linear combination of φ_{l+1} and φ_{l-1}. Specifically, the meridional structure of the ρ field for a long-wavelength $l = 1$ Rossby wave (the primary wave of interest here) is

$$\Phi_{nl}(\eta) = \frac{-1}{2\sqrt{2}}\left(\frac{\phi_2}{\sqrt{2}} + \phi_0\right) = \frac{1}{2\sqrt{2}\,\pi^{1/4}}(1 + 2\eta^2)e^{-\eta^2/2}, \tag{A2}$$

which has two off-equatorial relative maxima at the locations $y_m = \pm\sqrt{3/2}\sqrt{c/\beta}$.

As indicated in (A1), the double sum can be summed over n to produce the components $q_l(x, y, z, t)$. Note that each of these components is composed of waves only of a particular type l. The waves for the indices $l = -1$ and $l = 0$ are the Kelvin and Rossby–gravity waves, respectively, and those for $l \geq 1$ are Rossby waves. For this reason, when $l \geq 1$ we refer to q_l as being the lth Rossby wave of the solution. These Rossby waves can have quite simple vertical structures; in particular, they exhibit vertical phase and energy propagation and can be detected in the solutions reported in the main body of the text [see McCreary (1984) for a complete discussion].

Ray theory provides a useful method for determining where much of the energy associated with the lth Rossby wave will go. In this approach, the vertical structure functions $\Psi_n(z)$ in (A1) are replaced by their WKB approximation in the form $\exp\{imz\}$, where $m(z)$ is a "local" vertical wavenumber. The characteristic velocity c_n of each vertical mode is replaced by the WKB estimate $c = N_b/|m|$ (Gill 1982). The dispersion relation for equatorial Rossby waves is

$$\omega = \frac{-\beta k}{k^2 + (2l+1)\beta/c}, \tag{A3}$$

where k is the zonal wavenumber, and l is an integer ≥ 1. For long zonal wavelengths where $k^2 \approx 0$, the dispersion relation reduces to

$$\omega = \frac{-kc}{2l+1}. \tag{A4}$$

With $c = N_b/|m|$, (A4) becomes

$$\omega = \frac{-kN_b}{|m|(2l+1)}, \tag{A5}$$

and the usual ray equations (LeBlond and Mysak 1978, chapter 6) give the slope of ray paths in the (x, z) plane to be

$$\frac{dz}{dx} = \frac{dz/dt}{dx/dt} = \frac{\partial\omega/\partial m}{\partial\omega/\partial k} = \frac{(2l+1)\omega}{N_b(z)}\left(\frac{m}{|m|}\right). \tag{A6}$$

According to (A6), phase propagates *upward* across a band of energy propagating *downward* to the west (energy originating at the surface propagates downward to the west), with steeper slope for weaker stratification or higher meridional mode number l. Phase propagation in the zonal and vertical directions is, by definition, $c_p^x \equiv \omega/k$ and $c_p^z \equiv \omega/m$, so lines of constant phase have the slope $-c_p^z/c_p^x$. Because (A5) is nondispersive, this slope has the same value as the right-hand side of (A6). Thus, phase lines are parallel to WKB ray paths.

REFERENCES

Eriksen, C. C., 1981: Deep currents and their interpretation as equatorial waves in the western Pacific Ocean. *J. Phys. Oceanogr.*, **11,** 48–70.

Gent, P. R., 1985: The annual cycle in the central equatorial Pacific Ocean. *J. Mar. Res.*, **43,** 743–759.

——, and J. R. Luyten, 1985: How much energy propagates vertically in the equatorial oceans? *J. Phys. Oceanogr.*, **15,** 997–1007.

Gill, A. E., 1982: *Atmosphere–Ocean Dynamics.* Academic Press, 621 pp.

Hellerman, S., and M. Rosenstein, 1983: Normal monthly wind stress over the World Ocean with error estimates. *J. Phys. Oceanogr.*, **13,** 1093–1104.

Horigan, A. M., and R. H. Weisberg, 1981: A systematic search for trapped equatorial waves in the GATE velocity data. *J. Phys. Oceanogr.*, **11,** 497–509.

Kessler, W. S., 1990: Observations of long Rossby waves in the northern tropical Pacific. *J. Geophys. Res.*, **95,** 5183–5217.

——, 1991: Can reflected extraequatorial Rossby waves drive ENSO? *J. Phys. Oceanogr.*, **21,** 444–452.

——, and B. A. Taft, 1987: Dynamic heights and zonal geostrophic transports in the central tropical Pacific during 1979–84. *J. Phys. Oceanogr.*, **17,** 97–122.

Kubota, M., and J. J. O'Brien, 1988: Variability of the upper tropical Pacific Ocean model. *J. Geophys. Res.*, **93,** 13 930–13 940.

LeBlond, P., and L. Mysak, 1978: *Waves in the Ocean.* Elsevier Scientific, 602 pp.

Levitus, S., 1982: Climatological Atlas of the World Ocean. NOAA Prof. Paper 13, 173 pp. [U.S. Govt. Printing Office, Washington, D.C.]

Lukas, R., and E. Firing, 1985: The annual Rossby wave in the central equatorial Pacific Ocean. *J. Phys. Oceanogr.*, **11,** 55–67.

Luyten, J. R., and D. H. Roemmich, 1982: Equatorial currents at semiannual period in the Indian Ocean. *J. Phys. Oceanogr.*, **12,** 406–413.

McCreary, J. P., 1980: Modelling wind-driven ocean circulation. HIG Tech. Rep. HIG-80-3, 64 pp. [Hawaii Institute of Geophysics, Honolulu, HI.]

——, 1981: A linear stratified model of the equatorial undercurrent. *Phil. Trans. Roy. Soc. London A,* **278,** 603–635.

——, 1984: Equatorial beams. *J. Mar. Res.*, **42,** 395–430.

McPhaden, M. J., 1981: Continuously stratified models of the steady state equatorial ocean. *J. Phys. Oceanogr.*, **11,** 337–354.

——, J. Proehl, and L. M. Rothstein, 1986: The interaction of equatorial Kelvin waves with realistically sheared zonal currents. *J. Phys. Oceanogr.*, **16,** 1499–1515.

Meyers, G., 1979: Annual variation in the slope of the 14°C isotherm along the equator in the Pacific Ocean. *J. Phys. Oceanogr.*, **9,** 885–891.

Moore, D. W., and S. G. H. Philander, 1977: Modeling of the tropical ocean circulation. *The Sea,* Vol. 6, Wiley-Interscience, 319–361.

Proehl, J., 1990: Equatorial wave–mean flow interaction: The long Rossby waves. *J. Phys. Oceanogr.*, **20,** 274–294.

Rasmusson, E. M., and T. H. Carpenter, 1982: Variations in tropical sea surface temperature and surface wind fields associated with the Southern Oscillation/El Niño. *Mon. Wea. Rev.*, **110,** 354–384.

Rothstein, L. M., 1984: A model of the equatorial sea surface temperature field and associated circulation dynamics. *J. Phys. Oceanogr.*, **14,** 1875–1892.

——, D. W. Moore, and J. P. McCreary, 1985: Interior reflections of a periodically forced equatorial Kelvin wave. *J. Phys. Oceanogr.*, **15,** 985–996.

Weisberg, R. H., and A. M. Horigan, 1981: Low-frequency variability in the equatorial Atlantic. *J. Phys. Oceanogr.*, **11,** 913–920.

——, and T. Y. Tang, 1983: Equatorial ocean response to growing and moving wind systems with application to the Atlantic. *J. Mar. Res.*, **41,** 461–486.

——, ——, and C. Colin, 1979: Mixed Rossby–gravity wave propagation in the Gulf of Guinea. *J. Mar. Res.*, **37,** 67–86.

Wunsch, C., 1977: Response of an equatorial ocean to a periodic monsoon. *J. Phys. Oceanogr.*, **7,** 497–511.